Battery Adaptive Observer for a Single-Particle Model With Intercalation-Induced Stress

Dong Zhang[®], Satadru Dey[®], Member, IEEE, Luis D. Couto[®], and Scott J. Moura[®], Member, IEEE

Abstract—Battery electrode particle fracture due to stress generation is a critical mechanism causing capacity fade, and thus reducing battery life. This paper develops a nonlinear adaptive observer for lithium-ion battery state of charge (SOC), electrode particle stress, and solid phase diffusivity estimation using a high-fidelity coupled single particle-mechanical stress model, where the stress submodel captures stress development during lithium-ion intercalation and deintercalation. Simultaneous state and parameter estimation based on coupled single particle and mechanical stress model is extremely challenging because the coupled model is given by highly nonlinear partial differential equations. We address this problem by reducing the coupled model to a nonlinear finite dimensional system. The key novelty of this paper is a nonlinear internal state and parameter estimation methodology, from which the internal stress and the state of health-related parameters are monitored from real-time electric current and terminal voltage measurements. Numerical studies on simulation and experimental data have been conducted to illustrate the performance of the proposed estimation scheme.

Index Terms—Adaptive observer, electrochemical modeling, Li-ion batteries, Lyapunov stability, mechanical stress.

I. INTRODUCTION

AFE operation and degradation of lithium-ion (Li-ion) batteries have always been critical, especially when the usage of batteries gets ubiquitous. To address this problem, a battery management system (BMS) implements real-time control and estimation algorithms to enhance performance while improving safety [1]. One of the important functions of a BMS is battery SOC and state of health (SOH) estimation. However, simultaneous SOC and SOH estimation are particularly challenging due to: 1) limited real-time measurements; 2) complex electrochemical-thermal-mechanical physics; and

Manuscript received April 19, 2018; revised December 17, 2018; accepted March 21, 2019. Date of publication April 30, 2019; date of current version June 11, 2020. Manuscript received in final form April 9, 2019. Recommended by Associate Editor A. G. Stefanopoulou. (Corresponding author: Dong Zhang.)

D. Zhang is with the Department of Civil and Environmental Engineering, University of California at Berkeley, Berkeley, CA 94720 USA (e-mail: dongzhr@berkeley.edu).

- S. Dey is with the Department of Electrical Engineering, University of Colorado Denver, Denver, CO 80204 USA (e-mail: satadru.dey@ucdenver.edu).
- L. D. Couto is with the Department of Control Engineering and System Analysis, Université Libre de Brussels, B-1050 Brussels, Belgium (e-mail: lcoutome@ulb.ac.be).
- S. J. Moura is with the Department of Civil and Environmental Engineering, University of California at Berkeley, Berkeley, CA 94720 USA, and also with the Smart Grid and Renewable Energy Laboratory, Tsinghua-Berkeley Shenzhen Institute, Shenzhen 518055, China (e-mail: smoura@berkeley.edu).

Color versions of one or more of the figures in this article are available online at http://ieeexplore.ieee.org.

Digital Object Identifier 10.1109/TCST.2019.2910797

3) limitations of control theory—especially for nonlinear partial differential equation (PDE) models.

Battery models are typically used in a BMS for inferring internal states based on measured current, voltage, and temperature [2], [3]. The equivalent circuit models possess simple structure but sacrifice the information of internal states, while high-fidelity electrochemical models can capture the underlying physical and chemical processes [4]. Though electrochemical models accurately predict the internal states, their mathematical structures are often very complicated for control/estimation design. This point motivates model reduction techniques to reduce the complexity of full-order electrochemical models. Among the numerous reduced order models, the single-particle model (SPM) is the most commonly used one. The SPM is derived from the full-order electrochemical model, and hence it inherits some important properties. Each electrode of the SPM is assumed to be a single spherical particle, and the current distribution is uniform across both electrodes. In addition, the electrolyte concentration is assumed to be constant in space and time [3]. Based on the SPM, Kalman filter (KF) for SOC estimation was designed in [5] and [6]. The shortcoming of KF approaches arises from the difficulties to verify the asymptotic convergence properties. Lotfi et al. [7] proposed an SOC estimation technique using the SPM, where the radial domain dependence of solid phase lithium concentration is approximated by a fourth-order polynomial. One of the important drawbacks of the SPM is that it does not accurately predict voltage at high C-rate, since the electrolyte dynamics are neglected. In order to compensate this, models that combine the SPM with other components are developed. For instance, electrolyte phase contribution is approximated by polynomial functions in [8]. State estimation scheme with provable convergence for the SPM with electrolyte dynamics is derived and analyzed in [9]. Temperature distribution inside the battery is a crucial quantity for thermal management in BMS. An electrochemical model coupled with electrolyte dynamics and temperature-dependent parameters is presented for SOC estimation [10]. Battery SOC and internal temperature are estimated from a reduced and reformulated electrochemical model in [11].

In recent years, battery SOH has gained increased focus due to concerns over battery safety and life. Various factors contribute toward battery degradation, e.g., capacity fade and resistance growth. See [12] for a particularly excellent review. Though simultaneous SOC and SOH estimation problem has been well studied using circuit models [13]–[15], it is less examined for electrochemical models.

1063-6536 © 2019 IEEE. Personal use is permitted, but republication/redistribution requires IEEE permission. See https://www.ieee.org/publications/rights/index.html for more information.

Moura et al. [16] created an adaptive PDE observer for combined SOC and SOH estimation by adopting PDE backstepping observer design procedure. A nonlinear Luenberger-type adaptive observer is designed on a coupled electrochemical—thermal model in [17]. In the aforementioned papers, certain parameters, e.g., diffusion coefficient and contact resistance, are used as indicators of SOH, and these parameters are identified in real time.

Other than the model parameter-dependent health indicator for Li-ion batteries, this paper inspects another quantity for studying battery health, namely, the intercalation-induced stress generated inside the solid phase particles. An important capacity fade mechanism is the particle fracture due to intercalation- and deintercalation-induced stresses [18]. Volume changes of the electrode particles due to stress generation may induce particle fracture if the stress (radial or tangential [19], [20]) exceeds the yielding stress of the material [21]. This phenomenon motivates the development of models that incorporate stress mechanics into the SPM. Seminal work conducted by Christensen and Newman developed a mathematical model to capture volume expansion and contraction during lithium insertion [21]. Later, models that combine the SPM with diffusion-induced stress was introduced in [22], relying on an analogy to thermal stress. In [23], a modified SPM that incorporates stress-enhanced diffusion and electrolyte concentration distribution was developed. This model strikes an intriguing balance of fidelity and structural simplicity. An interesting BMS application of these models is introduced in [24], where the authors performed optimal charging under stress constraints. It is worth noting that spatial nonuniformity in battery electrode can cause degradation even when operating within the manufacturer specified limits. Although applying the SPM-based model for battery SOH estimation and monitoring cannot capture this spatial distribution of degradation patterns due to heterogeneities in electrode geometry [25], we seek quantitative aggregated stress prediction to better understand battery SOH in this paper.

In summary, there now exists a keen interest to address the SOH estimation problem, and recent model developments on diffusion-induced stress can be enabling. However, no work currently exists on state and parameter estimation with coupled SPM-stress models to the best of our knowledge. In this paper, we extend our previous work [26] and design a nonlinear observer based on this coupled model to estimate the bulk SOC, the particle stress profile, and the anode lithium diffusivity from current and voltage measurements only. Consequently, the real-time electrochemical model parameter can be monitored as a battery health indicator, and the electrode stress supports the studies on several physical degradation phenomena associated with battery health. This contribution departs from previous works in estimation for battery models in the following ways.

 It makes one of the first attempts to exploit the stressenhanced electrochemical model for the estimation of internal stress on top of SOC and model parameters. This issue is relevant for batteries consisting of electrodes that tend to expand and fracture due to stress.

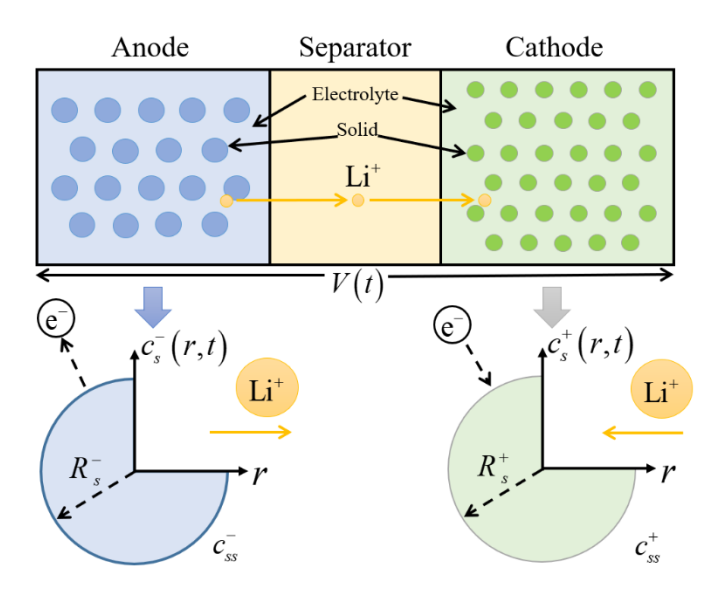


Fig. 1. Sketch of the SPM concept.

- 2) It considers a nonlinear state dynamical model stemming from intercalation-induced stress effects, which contrasts with linear state dynamics in [16] and [17].
- 3) A sliding mode observer-based adaptive estimation scheme is proposed, which differs from, e.g., output inversion and least-squares estimation [16]. The used observer is known to be robust against model uncertainties
- 4) It performs state and parameter estimation simultaneously while providing convergence conditions for the proposed estimation scheme through a rigorous stability analysis.

The remainder of this paper is organized as follows. Section II presents the battery SPM with intercalation-induced stress. Section III motivates the importance of monitoring the electrode stress via a simulation example. Section IV discusses model properties, model reduction, and state-space model formulation. The observer design with convergence analysis is presented in Section V. Section VI demonstrates the performance of the designed observer via simulation and utilizing experimental data. The limitations of the proposed scheme and future work are enumerated in Section VII. Finally, conclusions are drawn in Section VIII.

II. MODEL DESCRIPTION

Fig. 1 portrays the concept of the SPM. In the full-order electrochemical model (a.k.a. Doyle–Fuller–Newman model [4]), Li-ion transports in the solid and electrolyte phases. The key idea of the SPM is that the solid phase of each electrode can be modeled as a single spherical particle, and Li-ion concentration in electrolyte phase is assumed to be constant in space and time [16]. The SPM captures less dynamic behavior than the full-order model and specifically does not include mechanical responses, whose effect on diffusion becomes significant when the electrode material has high modulus and high partial molar volume [22].

TABLE I SPM-Stress Model Symbol Description

Symbols	Description	Units
a^{j}	Specific interfacial surface area	$[m^2/m^3]$
$\stackrel{A}{\circ}$	Cell cross sectional area	$[m^2]$
c_e^0	Li-ion concentration in electrolyte phase	[mol/m ³]
$c_{e}^{0} \ c_{s}^{j} \ c_{ss}^{j}$	Solid phase Li-ion concentration	[mol/m ³]
c_{ss}^{\jmath}	Li-ion concentration at particle surface	[mol/m ³]
$c_{s,\mathrm{max}}^{j}$	Max Li-ion concentration in solid phase	[mol/m ³]
$ ilde{c}_s^j$	Concentration change from stress-free value	[mol/m ³]
D_s^j	Solid phase diffusion coefficient	[m ² /sec]
E^j	Young's Modulus	[GPa]
F	Faraday's constant	[C/mol]
$D_s^j \ E^j \ F \ i_n^j \ I$	Particle surface current density	$[A/m^2]$
	Applied current	[A]
k^{j}	Charge transfer reaction rate	$[A \cdot m^{2.5}/mol^{1.5}]$
L^j	Electrode thickness	[m]
$n_{Li,s}$	Lithium in the solid phase	[mol]
r	Radial coordinate	[m]
R	Universal gas constant	[J/mol-K]
$R_{f_{\cdot}}$	Contact film resistance	[Ohm]
R_s^{\jmath}	Particle radius	[m]
t	Time	[Second]
T_{\parallel}	Battery cell temperature	[K]
U^j	Open circuit potential	[V]
Θ_{\min}^{j}	Lower stoichiometry point	[-]
Θ_{\max}^{j}	Upper stoichiometry point	[-]
$egin{array}{c} lpha^j \ arepsilon_s^j \ u^j \end{array}$	Charge transfer coefficient	[-]
$arepsilon_s^j$	Volume fraction of solid phase	[-]
	Poisson's ratio	[-]
$\sigma_h^j \ \Omega^j$	Hydrostatic stress	[MPa]
Ω^{j}	Partial molar volume	[mol/m ³]

The model equations for the coupled SPM and stress presented here closely follow the derivation by Zhang *et al.* [22]. A list of description for symbols can be found in Table I. For the case of a 2-D spherical particle, the intercalation of Li-ions in the solid phase is modeled as a process due to diffusion and stress generation, given by

$$\frac{\partial c_s^j}{\partial t} = D_s^j \left[\frac{\partial^2 c_s^j}{\partial r^2} - \frac{\Omega^j}{RT} \frac{\partial c_s^j}{\partial r} \frac{\partial \sigma_h^j}{\partial r} - \frac{\Omega^j}{RT} c_s^j \left(\frac{\partial^2 \sigma_h^j}{\partial r^2} + \frac{2}{r} \frac{\partial \sigma_h^j}{\partial r} \right) \right]$$
(1)

with the boundary condition

$$-D_{s}^{j}\left[\frac{\partial c_{s}^{j}}{\partial r}\left(R_{s}^{j},t\right)-\frac{\Omega^{j}}{RT}c_{s}^{j}\left(R_{s}^{j},t\right)\frac{\partial \sigma_{h}^{j}}{\partial r}\left(R_{s}^{j},t\right)\right]=\frac{i_{n}^{j}(t)}{F}$$
(2)

where $c_s^j = c_s^j(r,t) : [0,R_s^j] \times [0,\infty) \to \mathbb{R}$ maps the radial position and time to solid phase lithium concentration in electrode j, and $\sigma_h^j = \sigma_h^j(r,t) : [0,R_s^j] \times [0,\infty) \to \mathbb{R}$ maps the radial position and time to hydrostatic stress in electrode j. The current density i_n^j is proportional to the input current by the relation $i_n^j(t) = \pm I(t)/a^j A L^j$.

The stress tensor consists of radial stress σ_r and tangential stress σ_t , which are functions of the lithium concentration

$$\sigma_r^j(r,t) = 2\beta^j \left[\frac{1}{(R_s^j)^3} \int_0^{R_s^j} \tilde{c}_s^j r^2 dr - \frac{1}{r^3} \int_0^r \tilde{c}_s^j \rho^2 d\rho \right]$$
(3)
$$\sigma_t^j(r,t) = \beta^j \left[\frac{2}{(R_s^j)^3} \int_0^{R_s^j} \tilde{c}_s^j r^2 dr + \frac{1}{r^3} \int_0^r \tilde{c}_s^j \rho^2 d\rho - \tilde{c}_s^j \right]$$
(4)

where $\beta^j = \Omega^j E^j/3(1 - v^j)$. The hydrostatic stress is a weighted sum of σ_r and σ_t

$$\sigma_h^j = \frac{\sigma_r^j + 2\sigma_t^j}{3} = \frac{2}{3}\beta^j \left[\frac{3}{(R_s^j)^3} \int_0^{R_s^j} \tilde{c}_s^j r^2 dr - \tilde{c}_s^j \right]. \quad (5)$$

Substituting (5) into (1) yields

$$\frac{\partial c_s^j}{\partial t} = D_s^j \left[\left(1 + \theta^j c_s^j \right) \left(\frac{\partial^2 c_s^j}{\partial r^2} + \frac{2}{r} \frac{\partial c_s^j}{\partial r} \right) + \theta^j \left(\frac{\partial c_s^j}{\partial r} \right)^2 \right]$$
(6)

where $\theta^j = (\Omega^j/RT)[(2\Omega^j E^j)/9(1-\nu^j)]$ is a constant depending on electrode material mechanical properties. The boundary condition is obtained by substituting (5) into (2)

$$-D_s^j \left(1 + \theta^j c_s^j \left(R_s^j, t\right)\right) \frac{\partial c_s^j}{\partial r} \left(R_s^j, t\right) = \frac{\pm I(t)}{Fa^j AL^j}.$$
 (7)

For well-posedness, the Neumann boundary condition at r = 0 is required

$$\frac{\partial c_s^j}{\partial r}(0,t) = 0. (8)$$

The two variables, concentration and stress involved in PDE (1), are decoupled into a single nonlinear PDE (6) that describes the diffusion of Li-ion under the influence of stress, and concentration-dependent radial and tangential stresses in (3) and (4). Therefore, the dynamical equation for the solid phase Li-ion concentration with intercalation-induced stress is given by (6), with the boundary conditions (7) and (8). The nonlinearities in PDE (6) can be regarded as a diffusion with state-dependent diffusivity as well as a square of the spatial derivative of the state. Note that the intercalation-induced stress effect is ignored if $\theta^j = 0$, resulting in the regular SPM.

The output terminal voltage V_T is a function of solid phase surface concentration, open-circuit potentials (OCP), electric overpotentials, and Butler-Volmer kinetics

$$V_{T}(t) = \frac{RT}{\alpha^{+}F} \sinh \left[\frac{-I(t)}{2a^{+}AL^{+}i_{0}^{+}(c_{ss}^{+}(t))} \right]$$
$$-\frac{RT}{\alpha^{-}F} \sinh \left[\frac{I(t)}{2a^{-}AL^{-}i_{0}^{-}(c_{ss}^{-}(t))} \right]$$
$$+U^{+}(c_{ss}^{+}(t)) - U^{-}(c_{ss}^{-}(t)) - R_{f}I(t) \qquad (9)$$

where the exchange current density $i_0^j(\cdot)$ is

$$i_0^j(c_{ss}^j) = k^j \sqrt{c_e^0 c_{ss}^j(t) (c_{s,\text{max}}^j - c_{ss}^j(t))}$$
 (10)

$$c_{ss}^{j}(t) = c_{s}^{j}(R_{s}^{j}, t). \tag{11}$$

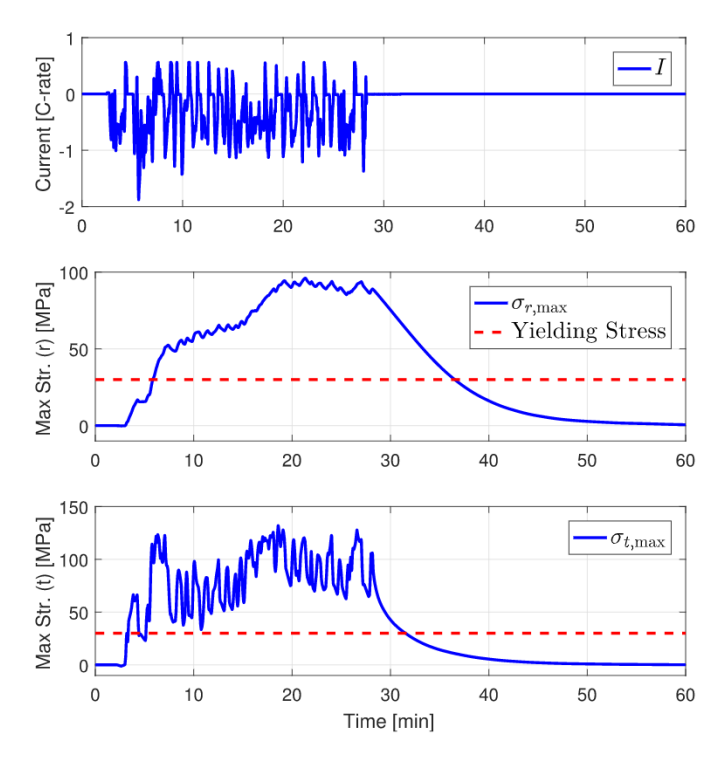


Fig. 2. Maximum radial and tangential stresses for a commercial NMC cell under UDDS cycle loads.

 $U^+(\cdot)$ and $U^-(\cdot)$ in (9) are the equilibrium potentials of positive and negative electrode material as functions of solid phase surface concentrations.

III. MOTIVATION

In this section, we illustrate the importance of monitoring stress inside the electrode solid particle via a simulation study. The model parameters are identified from the experimental data presented in Fig. 7 in Section VI-B, and they correspond to a commercial LiNiMnCoO₂ (NMC) - LiC₆ cell. A transient electric vehicle like charge/discharge cycle generated from urban dynamometer driving schedule (UDDS) is applied, and the maximum absolute radial and tangential stresses for anode (graphite) are simulated and plotted in Fig. 2. The maximum absolute radial and tangential stresses are located at the center and the surface of the electrode particle, respectively [22], and they are dependent on the change of radial Li-ion concentration from its stress-free value

$$\sigma_{r,\max}^{-}(t) = 2\beta^{-} \left[\frac{1}{\left(R_{s}^{-}\right)^{3}} \int_{0}^{R_{s}^{-}} \tilde{c}_{s}^{-} r^{2} dr - \frac{1}{3} \tilde{c}_{s}^{-}(0,t) \right]$$
(12)
$$\sigma_{t,\max}^{-}(t) = \beta^{-} \left[\frac{3}{\left(R_{s}^{-}\right)^{3}} \int_{0}^{R_{s}^{-}} \tilde{c}_{s}^{-} r^{2} dr - \tilde{c}_{s}^{-} \left(R_{s}^{-}, t\right) \right].$$
(13)

The red dotted lines in Fig. 2 represent the yielding stress for graphite. It is evident that the yielding stresses of materials are generally lowered by repeated cycling, and it is possible that the yielding stress of carbonaceous materials will fall below 30 MPa when the cell is cycled [21]. Consequently, the maximum absolute radial and tangential stresses exceed the yielding stress at approximately 4 and 1.2 min after the current

switches to nonzero value, respectively. The anode particle may fracture during the large portion of this driving cycle since the maximum stresses are significantly higher than the yielding stress. Hence, from the safety point of view, the users of the BMS shall greatly benefit from the real-time particle stress information to ensure safe operation and longevity of the battery.

Remark 1: The electrode particles are very likely to fracture if the maximum stresses exceed the yielding stress of the electrode material. However, the stresses at which particles actually fracture may greatly vary, and the yielding stress of the material is an upper limit on the stress required for particle fracture. It is possible to fracture during cycling even when the maximum stress is below the yielding stress [27]. Although the exact condition for particles to fracture may not be determined, criteria for electrode fracture tendency have been identified in [20], namely, strength-based and energy-based criteria.

IV. MODEL ANALYSIS AND REDUCTION

This section presents model properties, system observability analysis, and state-space formulation for observer design.

A. Conservation of solid-phase lithium

The moles of lithium in the solid phase $n_{Li,s}$ are conserved, where

$$n_{Li,s}(t) = \sum_{j \in \{+,-\}} \frac{\varepsilon_s^j L^j A}{\frac{4}{3}\pi \left(R_s^j\right)^3} \int_0^{R_s^j} 4\pi r^2 c_s^j(r,t) dr. \quad (14)$$

The lithium conservation can be verified by differentiating (14) with respect to time

$$\frac{d}{dt}n_{Li,s} = \sum_{j \in \{+,-\}} \frac{\varepsilon_s^j L^j A}{\frac{4}{3}\pi \left(R_s^j\right)^3} \int_0^{R_s^j} 4\pi r^2 \frac{\partial c_s^j(r,t)}{\partial t} dr$$

$$= \sum_{j \in \{+,-\}} \frac{D_s^j \varepsilon_s^j L^j A}{\frac{4}{3}\pi \left(R_s^j\right)^3} \int_0^{R_s^j} 4\pi r^2$$

$$\times \left[\theta^j \left(\frac{\partial c_s^j}{\partial r} \right)^2 + \left(1 + \theta^j c_s^j\right) \left(\frac{\partial^2 c_s^j}{\partial r^2} + \frac{2}{r} \frac{\partial c_s^j}{\partial r} \right) \right] dr$$

$$= \sum_{j \in \{+,-\}} \frac{3D_s^j \varepsilon_s^j L^j A}{R_s^j} \left[\left(1 + \theta^j c_s^j \left(R_s^j, t\right)\right) \frac{\partial c_s^j \left(R_s^j, t\right)}{\partial r} \right]$$

$$= \sum_{j \in \{+,-\}} -\frac{3D_s^j \varepsilon_s^j L^j A}{R_s^j} \frac{\pm I}{D_s^j F a^j A L^j}$$

$$= \frac{I}{F} - \frac{I}{F} = 0 \tag{15}$$

where the second equality comes from the dynamical equation (6), the third equality follows from integration by parts, the fourth equality results from the boundary conditions (7), and the last equality utilizes the relation $\varepsilon^j = a^j R_s^j/3$.

The lithium conservation property will be leveraged for model reduction in Section IV-B.

B. Model Reduction

The cell voltage in (9) depends on $U^+(c_{ss}^+) - U^-(c_{ss}^-)$, which makes the difference of the OCP observable from the voltage measurement but does not guarantee the observability of each OCP [6]. This paper adopts the idea in [6] to overcome this issue by seeking a relation between the positive and negative solid phase surface concentrations by the lithium conservation property in (14)

$$c_{ss}^{+} = \frac{n_{Li} - \varepsilon_s^{-} L^{-} a c_{ss}^{-}}{\varepsilon_s^{+} L^{+} A}$$
 (16)

and the output function (9) can be adjusted accordingly

$$V_{T}(t) = \frac{RT}{\alpha + F} \sinh \left[\frac{-I(t)}{2a + AL + i_{0}^{+} (\gamma c_{ss}^{-}(t) + \kappa)} \right]$$
$$-\frac{RT}{\alpha - F} \sinh \left[\frac{I(t)}{2a - AL - i_{0}^{-} (c_{ss}^{-}(t))} \right]$$
$$+ U^{+} (\gamma c_{ss}^{-}(t) + \kappa) - U^{-} (c_{ss}^{-}(t)) - R_{f} I(t) \quad (17)$$

where $\gamma = -(\varepsilon_s^- L^-)/(\varepsilon_s^+ L^+)$ and $\kappa = n_{Li}/(\varepsilon_s^+ L^+ A)$. The reduced system is then modeled by the anode dynamics $(c_s^-$ -system) from diffusion equation (6) and output function (17). Ideally, we intend to check the observability of the reduced nonlinear PDE system (6) and (17), but the theoretical results of the PDE system observability is not well developed, and as a result, we discretize the PDE system into a system of ordinary differential equations (ODEs) in the following section and evaluate the local observability of the spatially discretized system.

Remark 2: In this paper, we introduce state and parameter observer for the graphite anode in particular. Although the above model reduction is motivated by the observability condition from a control theory perspective, the anode selection arises from the physics. The graphite anodes are prone to degradation due to volume changes and concentration gradients [28]–[30], and such degradation results in diffusion-induced stress that might lead to particle fracture [21], [31].

C. State-Space Model Formulation and Analysis

There is a growing but small body of theoretical results on adaptive estimation of parabolic PDEs. For instance, an extended Luenberger-type observer is designed for a class of semilinear parabolic PDEs in [32], achieving exponential stability of the linearized observer error dynamics. However, the model therein reflects only semilinearity and no parameter uncertainties. The methods introduced in [33] stands out as it provides a thorough analysis and proof of adaptive scheme using output feedback for linear parabolic PDEs with spatially varying coefficients. Nonetheless, this approach does not directly extend to this paper as the SPM-Stress model contains highly nonlinear components. Ahmed-Ali et al. [34] developed an adaptive boundary observer for parabolic PDEs with both domain and boundary parameter uncertainties, with convergence results, where the PDE is linear in the states and parameters, making it more tractable for the backstepping technique. In the context of battery applications, Ascencio derives an adaptive PDE observer for the SPM, including

a parameter estimate for the diffusion coefficient [35]. Sum-of-squares programming is used for solving the kernel PDE online. Although these results have advanced our understanding of adaptive estimation for parabolic PDEs in infinite dimensional space, the considered problem in this paper is still extremely difficult. Hence, this paper uses model discretization so that finite dimensional estimation tools can be leveraged.

Henceforth, we will only consider dynamics for anode and drop the subscripts and superscripts to simplify notation, namely, $c = c_s^-$, $D = D_s^-$, $R_s = R_s^-$, $a = a^-$, $L = L^-$, and $\theta = \theta^-$. Suppose (N+1) nodes are used for discretization in the r direction, and $\Delta r = R_s/N$. Define the parameter

$$\tau = \frac{D}{(\Delta r)^2}. (18)$$

The central difference method is used for discretizing the PDEs into ODEs. The system of ODEs for the internal nodes of the anode diffusion dynamics is

$$\frac{\partial c_i}{\partial t} = \tau \left[(1 + \theta c_i)(c_{i-1} - 2c_i + c_{i+1}) + \left(\frac{2}{i} + \theta \frac{c_{i+1} - c_{i-1}}{2} + \frac{2\theta}{i} c_i \right) \left(\frac{c_{i+1} - c_{i-1}}{2} \right) \right]$$
(19)

where $i \in \{1, 2, ..., N-1\}$. At the right boundary point i = N $(r = R_s)$, the method of imaginary points is utilized to discretize the governing equations

$$\frac{\partial c_{N}}{\partial t} = \tau \left[(1 + \theta c_{N}) \left(c_{N-1} - c_{N} - \frac{I \cdot N}{3\tau \varepsilon \text{FAL}(1 + \theta c_{N})} \right) \right]
+ \tau \left[\frac{1}{N} + \frac{\theta}{4} \left(c_{N} - c_{N-1} - \frac{I \cdot N}{3\tau \varepsilon \text{FAL}(1 + \theta c_{N})} \right) + \frac{\theta}{N} c_{N} \right]
\cdot \left[c_{N} - c_{N-1} - \frac{I \cdot N}{3\tau \varepsilon \text{FAL}(1 + \theta c_{N})} \right].$$
(20)

The terms including 1/r has singularity at r = 0. Applying L'Hopital's rule eliminates the singularity, and (6) becomes

$$\frac{\partial c}{\partial t} = D \left[3(1 + \theta c) \frac{\partial^2 c}{\partial r^2} + \theta \left(\frac{\partial c}{\partial r} \right)^2 \right]. \tag{21}$$

Method of imaginary points can be employed again to discretize the governing equation at i = 0 (r = 0)

$$\frac{\partial c_0}{\partial t} = 6\tau (1 + \theta c_0)(c_1 - c_0). \tag{22}$$

The state-space model can be written in the following form based on (19), (20), (22), and (17)

$$\dot{x} = \tau A x + \tau \theta f(x, \tau, u)$$

$$y = h(c_N, u)$$
(23)

where the state vector $x = [c_0 \ c_1 \ c_2 \ \dots \ c_N]^{\top} \in \mathbb{R}^{N+1}$, input $u = I \in \mathbb{R}$ is the applied current, output terminal voltage $y = h(c_N, u) = V_T \in \mathbb{R}$, nonlinear function $f(x, \tau, u) = [f_0(x) \ f_1(x) \ \dots \ f_{N-1}(x) \ f_N(x, \tau, u)]^{\top} \in \mathbb{R}^{N+1}$, and

matrix $A \in \mathbb{R}^{(N+1)\times(N+1)}$. Following the derivation from (19), (20), and (22), we have

$$\mathcal{A} = \begin{bmatrix}
-6 & 6 & 0 & 0 & \cdots & \cdots & 0 \\
0 & -2 & 2 & 0 & \cdots & \cdots & 0 \\
0 & \frac{1}{2} & -2 & \frac{3}{2} & \cdots & \cdots & 0 \\
0 & 0 & \frac{2}{3} & -2 & \cdots & \cdots & 0 \\
\vdots & \vdots & \vdots & \ddots & \ddots & \ddots & \vdots \\
0 & 0 & 0 & 0 & \cdots & -2 & \frac{N}{N-1} \\
0 & 0 & 0 & 0 & \cdots & \frac{N-1}{N} & -\frac{N-1}{N}
\end{bmatrix}$$
(24)

and

$$f(x, \tau, u) = \begin{bmatrix} 6c_0(c_1 - c_0) \\ \vdots \\ c_i\left(\frac{i-1}{i}c_{i-1} - 2c_i + \frac{i+1}{i}c_{i-1}\right) + \frac{(c_{i+1} - c_{i-1})^2}{4} \\ \vdots \\ f_N(c_{N-1}, c_N, \tau, u) \end{bmatrix}$$

where

$$f_{N}(c_{N-1}, c_{N}, \tau, u) = -\frac{N+1}{\theta N} \frac{I \cdot N}{3\tau \varepsilon \text{FAL}(1+\theta c_{N})} + c_{N} \left[c_{N-1} - c_{N} - \frac{I \cdot N}{3\tau \varepsilon \text{FAL}(1+\theta c_{N})} \right] + \left[\frac{1}{4} \left(c_{N} - c_{N-1} - \frac{I \cdot N}{3\tau \varepsilon \text{FAL}(1+\theta c_{N})} \right) + \frac{1}{N} c_{N} \right] \times \left[c_{N} - c_{N-1} - \frac{I \cdot N}{3\tau \varepsilon \text{FAL}(1+\theta c_{N})} \right].$$
 (26)

Assumption 1: It has been verified by numerous literature [36] that the nonlinear output function $h(c_N, u)$ is strictly increasing with respect to the surface concentration c_N . We can conclude that for any given finite input u and any two different surface concentration values $c_{N,i}, c_{N,j} \in [\Theta_{\min}^-, \Theta_{\max}^-] \cdot c_{s,\max}^-$, the following expression holds:

$$sgn(h(c_{N,i}, u) - h(c_{N,i}, u)) = sgn(c_{N,i} - c_{N,i})$$
 (27)

where the operator $sgn(\cdot)$ is the signum function.

This property will become important, as it eases the analysis of observer convergence in the next section.

Remark 3: The function $f(x, \tau, u)$ is continuously differentiable with respect to the state x and the parameter τ , a sufficient condition for Lipschitz continuity [36]. For any two vectors $X_1, X_2 \in \mathbb{R}^{N+1}$, where each entry of X_1 and X_2 is within the range $[\Theta_{\max}^-, \Theta_{\min}^-] \cdot c_{s,\max}^-$, a Lipschitz constant with respect to the state x can be obtained by computing the infinity norm of $\partial f/\partial x$, i.e., $K_x = \|\partial f/\partial x\|_{\infty}$, such that

$$||f(X_1, \tau, u) - f(X_2, \tau, u)|| < K_x ||X_1 - X_2||.$$
 (28)

Similarly, for any two scalars T_1 , $T_2 \in \mathbb{R}$, a Lipschitz constant with respect to the parameter τ is expressed as $K_{\tau} = \|\partial f/\partial \tau\|_{\infty}$, such that

$$||f(x, T_1, u) - f(x, T_2, u)|| \le K_\tau ||T_1 - T_2||.$$
 (29)

From (28) and (29), a multivariable Lipschitz continuous condition for the function $f(x, \tau, u)$ is inferred

$$||f(X_1, T_1, u) - f(X_2, T_2, u)|| \le K_x ||X_1 - X_2|| + K_\tau ||T_1 - T_2||.$$
 (30)

It also immediately follows from (28) that $f_N(c_N, c_{N-1}, \tau, u)$ is bounded within the compact operating interval c_{N-1} , $c_N \in [\Theta_{\min}^-, \Theta_{\max}^-] \cdot c_{s,\max}^-$, for all finite input current u and finite parameter τ . Mathematically, for any (c_{N-1}, c_N) and (c_{N-1}', c_N')

$$|f_N(c_{N-1}, c_N, \tau, u) - f_N(c'_{N-1}, c'_N, \tau, u)| \le M$$
 (31)

where $0 < M < \infty$.

Remark 4: It should be pointed out that the considered setup can be readily transferred to the case of concentration-dependent parameters, e.g., D=D(c) and $\theta=\theta(c)$. Suppose the dependence is continuous, then the Lipschitz continuity property on nonlinear function $f(x,\tau,u)$ introduced in Remark 3 still holds since the discretized concentration c_i is bounded by $[\Theta_{\min}^-, \Theta_{\max}^-] \cdot c_{s,\max}^-$.

D. Observability Analysis

The observbility of a nonlinear finite-dimensional system can be verified by a rank test based on the concept of *Lie Derivatives*. It should be pointed out that the local observability of a nonlinear system is not equivalent to the observability of the linearized system, which was examined previously in [37] and [38] for battery equivalent circuit models. Here, we present local observability rank test by considering the following form of nonlinear system:

$$\dot{x} = \eta(x) + \sum_{i=1}^{m} u_i g_i(x)$$
 (32)

$$y = \phi(x) \tag{33}$$

where $x \in \mathbb{R}^n$ is the state, $u_i \in \mathbb{R}$ is the input, $y \in \mathbb{R}$ is the output, and η , g_i , and ϕ are real-valued smooth functions. The gradient of ϕ , denoted by $d\phi$, is expressed by

$$d\phi = \begin{bmatrix} \frac{\partial \phi}{\partial x_1} & \frac{\partial \phi}{\partial x_2} & \cdots & \frac{\partial \phi}{\partial x_n} \end{bmatrix}. \tag{34}$$

The Lie derivative of ϕ with respect to function η is denoted by

$$L_{\eta}\phi = d\phi \cdot \eta = \sum_{i=1}^{n} \frac{\partial \phi}{\partial x_{i}} \cdot \eta_{i}. \tag{35}$$

The following theorem [39] provides the rank test for local observability of a nonlinear system in the form of (32) and (33).

Theorem 1: Suppose $x_0 \in \mathbb{R}^n$ is given. Consider the expression

$$\Gamma = (dL_{7s}L_{7s-1}\cdots L_{71}\phi)(x_0) \tag{36}$$

where $s \ge 0$, $z_i \in \{\eta, g_1, \dots, g_m\}$, evaluated at x_0 . If there are n linearly independent row vectors in Γ , then the system is locally observable around x_0 .

Herein, for the simplicity of the calculation, we evaluate the local observability under constant input current. The expressions of $\eta(x)$, $g_1(x)$, $g_2(x)$, and $\phi(x)$ can be derived from the state-space model (23)–(26), and $u_1 = I$ and $u_2 = I^2$. The calculation of Γ in (36) reveals that the system is locally observable at x_0 .

V. OBSERVER DESIGN AND ANALYSIS

The state and parameter estimation problem seeks to design an adaptive observer system to reconstruct the unknown state x and parameter τ in the plant model (23) with the knowledge of output y and input u measurements. In this paper, the available energy of the battery cell is quantified by the bulk SOC in the anode, and it can be computed from normalizing the anode volume average of Li-ion concentration against the maximum concentration

$$SOC(t) = \frac{3}{(R_s^-)^3 c_{s,\text{max}}^-} \int_0^{R_s^-} r^2 c_s^-(r, t) dr.$$
 (37)

Note that the SOC calculation in (37) yields an unnormalized value. The actual bulk SOC should be normalized with respect to the difference of upper and lower stoichiometry points of anode material. The estimation of radial and tangential stresses is computed using solid phase Li-ion concentration estimation by (3) and (4).

Remark 5: The magnitude of diffusion-induced electrode stress is not a comprehensive indicator of battery health, but certainly is a contributor to several physical degradation phenomena associated with battery health. Examples include the growth of particle surface cracks as a function of maximum tangential stress according to Paris' Law [40], and mechanical fatigue described by the Palmgren–Milner (PM) rule [41].

The primary unknown parameter considered in this paper is the diffusivity in the anode D_s^- , or equivalently τ , as it directly affects the dynamics of Li-ion transportation in the solid phase. There is also consensus within the literature that the diffusion coefficient is one of the most sensitive parameters to the battery cycling aging [42]. Aside from improving the state estimation accuracy, the estimated parameter can be regarded as an indicator of SOH. Thus, the battery health condition is assessed by both model parameter values and physical degradation phenomena associated with the diffusion-induced stress.

Systematic ways for adaptive observer design for nonlinear systems have been studied in the existing literature [43], [44]. These approaches often consider certain dynamic model structures with linear model output function, where the linearity in the output is an essential property for deriving the update law for parameter estimate. Nonetheless, the output map in the battery application is highly nonlinear with respect to the states and input, which makes the adaptive observer design intricate. In this paper, we adopt a similar approach as in [43], with the extension to: 1) a nonlinear output equation and 2) a more general model dynamics structure. The stability

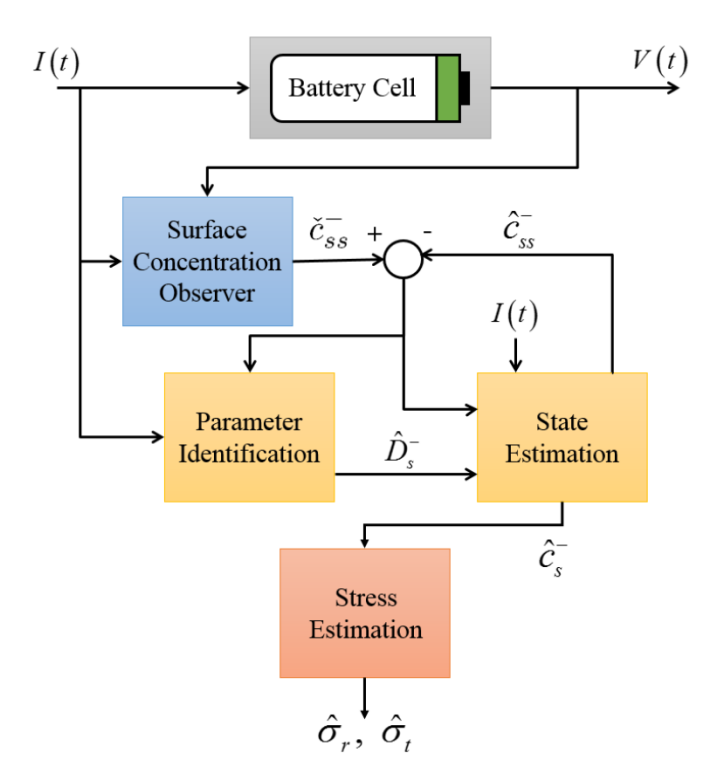


Fig. 3. Block diagram of adaptive observer structure. It consists of the solid phase surface concentration observer (blue), the adaptive observer (yellow), and the stress estimation calculation (coral). The adaptive observer is comprised of two parts: diffusion coefficient identification (yellow/left) and full-state observer (yellow/right). The observers utilize measurements of input current and output terminal voltage only.

of the proposed observer will be rigorously analyzed by Lyapunov's direct method.

Fig. 3 depicts the observer design concept. The surface concentration observer (blue block) takes the measurements of input current and output voltage to estimate the surface concentration only. The estimated surface concentration becomes a pseudomeasurement signal utilized in the subsequent adaptive observer (yellow blocks). The model used for adaptive observer design is reformulated such that the surface concentration estimation becomes the model output, which is a linear function of the state vector. Finally, the stress estimation (coral block) can be calculated from the state estimates. The details are illustrated in the following sections.

A. Surface Concentration Observer Design

In this section, we present the observer design for estimating solid phase surface concentration (blue block in Fig. 3), and the corresponding convergence analysis using Lyapunov's direct method.

In order to obtain surface concentration information and reformulate the state space model for adaptive observer design, we separate the state vector x into two components, namely, define $\xi = [c_0 \ c_1 \ \cdots \ c_{N-1}]^{\top}$ that contains the first N entries of x, and $x = [\xi^{\top} \ c_N]^{\top}$. Rewrite the plant model (23) as

$$\dot{\xi} = \tau \overline{\mathcal{A}} x + \tau F(x) \tag{38}$$

$$\dot{c}_N = \tau \frac{N-1}{N} c_{N-1} - \tau \frac{N-1}{N} c_N + \tau \theta f_N(x, u)$$
 (39)

$$y = h(c_N, u) \tag{40}$$

where matrix $\overline{\mathcal{A}}$ is the matrix \mathcal{A} excluding the last row, and $F(x) = [f_0(\xi) \ f_1(\xi) \ \cdots \ f_{N-1}(x)]^{\top}$. Note that in the plant model (38)–(40), the unknown parameter is τ and the unknown states are ξ and c_N . Despite the fact that τ is unknown, proper upper and lower bounds of τ are assumed. These bounds can be retrieved from existing literature based on the electrode materials. Mathematically, we have

$$0 < \underline{\tau} \le \tau \le \overline{\tau} < \infty. \tag{41}$$

Consider the following observer structure:

$$\dot{\check{c}}_{N} = \tau^{o} \frac{N-1}{N} \check{c}_{N-1} - \tau^{o} \frac{N-1}{N} \check{c}_{N} + \tau^{o} \theta \, \check{f}_{N}$$

$$+ L \cdot \operatorname{sgn}(y - \check{y})$$
(42)

where the quantities with the "inverse hat" symbols denote their estimation, and the scalar observer gain L>0 is to be designed such that the estimation converges to the actual value. Moreover, $\check{f}_N=f_N(\check{c}_{N-1},\check{c}_N,\tau^o,u)$. The parameter τ^o is a nominal value chosen a priori such that $\underline{\tau}\leq \tau_o\leq \overline{\tau}$, and we further assume that $\tau=\tau^o+\delta\tau$. Our objective is to estimate the surface concentration with the presence of parameter uncertainty, which can be achieved by selecting a sufficiently high observer gain L. The above-mentioned sliding mode observer structure adopts the error injection concept and is well known for its robustness against parameter/model uncertainty when applied to nonlinear systems [45].

Proposition 1: Consider the surface concentration dynamics (39) with bounded unknown parameter $\underline{\tau} \leq \tau \leq \overline{\tau}$, and observer (42). If there exists a scalar gain such that

$$L > \overline{\tau} \frac{N-1}{N} |\tilde{c}_{N-1}|_{\max} + \overline{\tau} \theta M + \overline{\Psi}$$
 (43)

in which $\overline{\Psi} > 0$ is finite and given by (45), then the estimation error $\tilde{c}_N = c_N - \check{c}_N$ converges to zero in finite time.

Proof: Consider the estimation errors $\tilde{c}_N = c_N - \check{c}_N$ and $\tilde{c}_{N-1} = c_{N-1} - \check{c}_{N-1}$. Subtracting (42) from (39), and the error dynamics can be written as

$$\dot{\tilde{c}}_{N} = \tau^{o} \frac{N-1}{N} \tilde{c}_{N-1} - \tau^{o} \frac{N-1}{N} \tilde{c}_{N} + \tau^{o} \theta \, \tilde{f}_{N} - L \operatorname{sgn}(\tilde{c}_{N})$$

$$+ \delta \tau \frac{N-1}{N} c_{N-1} - \delta \tau \frac{N-1}{N} c_{N} + \delta \tau \theta f_{N}$$
(44)

where $\tilde{f}_N = f_N(c_{N-1}, c_N, \tau, u) - f_N(\check{c}_{N-1}, \check{c}_N, \tau^o, u)$. Note that we have utilized the monotonicity property of y (see Assumption 1) to substitute $\operatorname{sgn}(y - \check{y})$ with $\operatorname{sgn}(\tilde{c}_N)$. Based on the fact that c_N , c_{N-1} , and f_N are bounded under finite input current, let

$$\Psi \triangleq \delta \tau \frac{N-1}{N} c_{N-1} - \delta \tau \frac{N-1}{N} c_N + \delta \tau \theta f_N \le \overline{\Psi} \quad (45)$$

with $\overline{\Psi} > 0$ being the upper bound of Ψ .

We analyze the error dynamics (44) using the Lyapunov function candidate

$$V = \frac{1}{2}\tilde{c}_N^2 \tag{46}$$

and the derivative of the Lyapunov function along the trajectory of \tilde{c}_N is

$$\dot{V} = \tilde{c}_{N}\dot{\tilde{c}}_{N}
= \tilde{c}_{N} \left[\tau^{o} \frac{N-1}{N} \tilde{c}_{N-1} - \tau^{o} \frac{N-1}{N} \tilde{c}_{N} + \tau^{o} \theta \, \tilde{f}_{N} \right]
- L \operatorname{sgn}(\tilde{c}_{N}) + \Psi
\leq |\tilde{c}_{N}| \left[\overline{\tau} \frac{N-1}{N} |\tilde{c}_{N-1}| + \overline{\tau} \theta |\tilde{f}_{N}| + \overline{\Psi} \right] - L \tilde{c}_{N} \operatorname{sgn}(\tilde{c}_{N})
- \tau^{o} \frac{N-1}{N} \tilde{c}_{N}^{2}
\leq |\tilde{c}_{N}| \left[\overline{\tau} \frac{N-1}{N} |\tilde{c}_{N-1}| + \overline{\tau} \theta |\tilde{f}_{N}| + \overline{\Psi} \right] - L |\tilde{c}_{N}|
\leq |\tilde{c}_{N}| \left[\overline{\tau} \frac{N-1}{N} |\tilde{c}_{N-1}| + \overline{\tau} \theta M + \overline{\Psi} - L \right].$$
(47)

If the gain L is chosen high enough such that

$$L > \overline{\tau} \frac{N-1}{N} |\tilde{c}_{N-1}|_{\text{max}} + \overline{\tau} \theta M + \overline{\Psi}$$
 (48)

then we have that $\dot{V}_1 \leq 0$.

Choose L^* that meets the condition in (48), and define

$$\rho = L^* - \left[\overline{\tau} \frac{N-1}{N} |\tilde{c}_{N-1}|_{\max} + \overline{\tau} \theta M + \overline{\Psi} \right] > 0. \quad (49)$$

From (47) and (49), we have that

$$\dot{V} \le -\sqrt{2}\rho\sqrt{V}.\tag{50}$$

The time required for \tilde{c}_N to converge to zero can be analytically computed by solving (50) for V using the comparison principle [46], and setting V=0 and solving for t_f

$$t_f = \frac{\sqrt{2V(0)}}{\rho} \tag{51}$$

where V(0) is the initial condition of V. Therefore, after $t \ge t_f$, $\tilde{c}_N \to 0$. Finite time convergence of $\check{c}_N \to c_N$ is attained.

B. Adaptive Observer Design

In this section, we develop the adaptive observer by extending the results from [43]. The surface concentration estimation \check{c}_N from the surface concentration observer is leveraged as a pseudomeasurement signal for a reformulated plant model. The dynamical equations in (23) are preserved while the output is reformulated as a linear function of the state vector

$$\dot{x} = \tau A x + \tau \theta f(x, \tau, u) \quad y_s = C x \tag{52}$$

where $y_s = c_N$ and $C = [0 \ 0 \ \cdots \ 0 \ 1] \in \mathbb{R}^{1 \times (N+1)}$. The adaptive observer is designed such that the unknown state x and parameter τ are converging to their actual values simultaneously. The estimation system consists of a copy of the plant model (52) plus the output error injection, as follows:

$$\dot{\hat{x}} = \hat{\tau} \mathcal{A} \hat{x} + \hat{\tau} \theta f(\hat{x}, \hat{\tau}, u) + L_a(y_s - \hat{y}_s)
\hat{y}_s = C \hat{x}$$
(53)

where the quantities with the "hat" symbols denote their estimation, and $L_a \in \mathbb{R}^{N+1}_+$ is a vector of positive scalar gains

to be designed. We seek to derive an update law for $\hat{\tau}$ and conditions on L_a that guarantee the convergence of state and parameter estimates. Theorem 1 summarizes the convergence results for adaptive observer (53).

Theorem 2: Consider the plant model (52) and observer system (53), given accurate estimation of surface concentration from Proposition 1. Let the error between the actual and the estimated quantities to be $\tilde{x} = x - \hat{x}$, $\tilde{\tau} = \tau - \hat{\tau}$, and $\tilde{y}_s = y_s - \hat{y}_s$. Furthermore, assume the actual value of the unknown parameter is bounded by $\underline{\tau} \leq \tau < \overline{\tau}$. Then, the estimation errors \tilde{x} and $\tilde{\tau}$ converge to zero asymptotically, if the observer gain vector L_a is designed such that for all $\tau^{\dagger} \in [\underline{\tau}, \overline{\tau}]$, there exists a positive semidefinite matrix Q that verifies

$$\tau^{\dagger} \mathcal{A} + \overline{\tau} \theta K_x I_N - L_a c \le -Q \tag{54}$$

and $\hat{\tau}$ evolves according to the system

$$\dot{\hat{\tau}} = \frac{\tilde{y}_s C A \hat{x} + \tilde{y}_s \theta f_N(\hat{x}, \hat{\tau}, u)}{\gamma}$$
 (55)

where I_N denotes a $(N+1) \times (N+1)$ identity matrix, and $\gamma > 0$.

Proof: The state error dynamics are expressed by subtracting (53) from (52)

$$\dot{\tilde{x}} = \tau A x - \hat{\tau} A \hat{x} + \tau \theta f(x, \tau, u) - \hat{\tau} \theta f(\hat{x}, \hat{\tau}, u) - L_a \tilde{y}_s$$

$$\tilde{y}_s = C \tilde{x}.$$
(56)

The Lyapunov function candidate is chosen as

$$V_a = \frac{1}{2}\tilde{x}^{\mathsf{T}}\tilde{x} + \frac{1}{2}\gamma\,\tilde{\tau}^2, \quad \text{where } \gamma > 0. \tag{57}$$

The derivative of V_a along the trajectory of \tilde{x} is

$$\dot{V}_{a} = \frac{1}{2}\dot{\tilde{x}}^{\top}\tilde{x} + \frac{1}{2}\tilde{x}^{\top}\dot{\tilde{x}} + \gamma\,\tilde{\tau}\dot{\tilde{\tau}} \\
= \tilde{x}^{\top}\dot{\tilde{x}} + \gamma\,\tilde{\tau}\dot{\tilde{\tau}} \\
= \tilde{x}^{\top}[\tau\mathcal{A}x - \hat{\tau}\mathcal{A}\hat{x} + \tau\theta f(x,\tau,u) - \hat{\tau}\theta f(\hat{x},\hat{\tau},u) \\
- L_{a}\tilde{y}_{s}] + \gamma\,\tilde{\tau}\dot{\tilde{\tau}} \\
= \tilde{x}^{\top}[\tau\mathcal{A}x - (\tau - \tilde{\tau})\mathcal{A}\hat{x} + \tau\theta f(x,\tau,u) \\
- (\tau - \tilde{\tau})\theta f(\hat{x},\hat{\tau},u) - L_{a}c\tilde{x}] + \gamma\,\tilde{\tau}\dot{\tilde{\tau}} \\
= \tilde{x}^{\top}[\tau\mathcal{A}\tilde{x} + \tilde{\tau}\mathcal{A}\hat{x} + \tau\theta (f(x,\tau,u) - f(\hat{x},\hat{\tau},u)) \\
+ \tilde{\tau}\theta f(\hat{x},\hat{\tau},u) - L_{a}c\tilde{x}] + \gamma\,\tilde{\tau}\dot{\tilde{\tau}} \\
\leq \tilde{\tau}[\tilde{x}^{\top}\mathcal{A}\hat{x} + \tilde{x}^{\top}\theta f(\hat{x},\hat{\tau},u) - \gamma\,\dot{\tilde{\tau}}] \\
+ \tilde{x}^{\top}(\tau\mathcal{A} - L_{a}c)\tilde{x} + \tau\theta \|\tilde{x}\| \|f(x,\tau,u) - f(\hat{x},\hat{\tau},u)\| \\
\leq \tilde{\tau}[\tilde{x}^{\top}\mathcal{A}\hat{x} + \tilde{x}^{\top}\theta f(\hat{x},\hat{\tau},u) - \gamma\,\dot{\tilde{\tau}}] \\
+ \tilde{x}^{\top}(\tau\mathcal{A} - L_{a}c)\tilde{x} + \overline{\tau}\theta \|\tilde{x}\| (K_{x}\|\tilde{x}\| + K_{\tau}\|\tilde{\tau}\|) \\
= \tilde{\tau}[\tilde{x}^{\top}\mathcal{A}\hat{x} + \tilde{x}^{\top}\theta f(\hat{x},\hat{\tau},u) - \gamma\,\dot{\tilde{\tau}}] \\
+ \tilde{x}^{\top}(\tau\mathcal{A} - L_{a}c)\tilde{x} + \overline{\tau}\theta \|\tilde{x}\| (K_{x}\|\tilde{x}\| + K_{\tau}\|\tilde{\tau}\|) \\
= \tilde{\tau}[\tilde{x}^{\top}\mathcal{A}\hat{x} + \tilde{x}^{\top}\theta f(\hat{x},\hat{\tau},u) - \gamma\,\dot{\tilde{\tau}}] \\
+ \tilde{x}^{\top}(\tau\mathcal{A} + \overline{\tau}\theta K_{x}I_{N} - L_{a}c)\tilde{x} + \overline{\tau}\theta K_{\tau}\|\tilde{x}\|\|\tilde{\tau}\|$$
 (58)

where we have applied the Lipschitz continuity of the function f with respect to x and τ at the second inequality according to Remark 3, and the last equality follows from $\|\tilde{x}\| \|\tilde{x}\| = \tilde{x}^{\top} \tilde{x}$.

Now, choose the update law for $\hat{\tau}$ by eliminating the terms associated with $\tilde{\tau}$ in the last line of (58)

$$\tilde{x}^{\top} \mathcal{A} \hat{x} + \tilde{x}^{\top} \theta f(\hat{x}, \hat{\tau}, u) - \gamma \dot{\hat{\tau}} = 0.$$
 (59)

Since \tilde{x} is unavailable because the actual states are unknown, we multiply both sides of (59) by $CC^{\top} = 1$ to get

$$\tilde{y}_s C \mathcal{A} \hat{x} + \tilde{y}_s C \theta f(\hat{x}, \hat{\tau}, u) - \gamma \dot{\hat{\tau}} = 0. \tag{60}$$

Then, the update law for $\hat{\tau}$ can be explicitly written as

$$\dot{\hat{\tau}} = \frac{\tilde{y}_s C A \hat{x} + \tilde{y}_s \theta f_N(\hat{x}, \hat{\tau}, u)}{\gamma}$$
 (61)

and the inequality (58) is simplified to

$$\dot{V}_a \le \tilde{x}^\top (\tau \mathcal{A} + \overline{\tau} \theta K_x I_N - L_a c) \tilde{x} + \overline{\tau} \theta K_\tau ||\tilde{x}|| ||\tilde{\tau}||.$$
 (62)

Choose gain L_a such that for all $\tau^{\dagger} \in [\underline{\tau}, \overline{\tau}]$, there exists a positive semidefinite matrix Q that satisfies

$$\tau^{\dagger} \mathcal{A} + \overline{\tau} \theta K_x I_N - L_a c \le -Q \tag{63}$$

and therefore,

$$\dot{V}_{a} \leq -\tilde{x}^{\top} Q \tilde{x} + \overline{\tau} \theta K_{\tau} \|\tilde{x}\| \|\tilde{\tau}\| \\
\leq -\lambda_{\min}(Q) \|\tilde{x}\|^{2} + \overline{\tau} \theta K_{\tau} \|\tilde{x}\| \|\tilde{\tau}\| \\
= -[\|\tilde{x}\| \|\tilde{\tau}\|] \begin{bmatrix} \lambda_{\min}(Q) & -\overline{\tau} \theta K_{\tau} \\ 0 & 0 \end{bmatrix} \begin{bmatrix} \|\tilde{x}\| \\ \|\tilde{\tau}\| \end{bmatrix} \\
\triangleq -\tilde{v} P \tilde{v}^{\top}$$
(64)

where $\tilde{v} = [\|\tilde{x}\| \|\tilde{\tau}\|]$. Apparently, the matrix P is positive semidefinite since the eigenvalues of P are $\{\lambda_{\min}(Q), 0\}$, where $\lambda_{\min}(Q) \geq 0$. Hence, it follows that $\dot{V}_a \leq 0$. Next, we analyze the convergence of state and parameter estimation errors.

1) Convergence of State Estimation: Integrating both sides of (64) and we have that

$$V_a(t) \le V_a(0) - \int_0^t \tilde{v}^\top P \tilde{v} dt \tag{65}$$

which implies $0 \le V_a(t) \le V_a(0)$, so $V_a \in L_{\infty}$. From (57), $\tilde{x} \in L_{\infty}$ and $\tilde{\tau} \in L_{\infty}$. Moreover, $\hat{x} = x - \tilde{x} \in L_{\infty}$ and $\hat{\tau} = \tau - \tilde{\tau} \in L_{\infty}$. Since $V_a(0)$ is finite and $V_a(t) \in L_{\infty}$, $\tilde{x} \in L_2$. In addition, from (56) and the fact that f is bounded, we have $\tilde{x} \in L_{\infty}$. According to Barbalat's Lemma [47], $\tilde{x}, \dot{\tilde{x}} \in L_{\infty}$ and $\tilde{x} \in L_2$ allows us to conclude that

$$\lim_{t \to \infty} \tilde{x} = 0. \tag{66}$$

Therefore, \hat{x} converges to x asymptotically.

2) Convergence of Parameter Estimation: It has been shown in the previous sections that \tilde{x} is differentiable and has a finite limit as $t \to \infty$. Since f is the Lipschitz continuous, f is immediately uniformly continuous. Let $\chi = \tau \mathcal{A}x - \hat{\tau}\mathcal{A}\hat{x} - L_a\tilde{y}_s = \tau \mathcal{A}\tilde{x} + \tilde{\tau}\mathcal{A}\hat{x} - L_aC\tilde{x}$, which are the terms at the right-hand side of (56) that are not associated with function f, and we would like to show χ is uniformly continuous by verifying the boundedness of $\dot{\chi}$. Taking the derivative of χ with respect to time

$$\dot{\chi} = \tau A \dot{\tilde{x}} + \dot{\tilde{\tau}} A \hat{x} + \tilde{\tau} A \dot{\hat{x}} - L_a c \dot{\tilde{x}}. \tag{67}$$

Since $\hat{x} \in L_{\infty}$ and f is bounded, we have $\dot{\hat{x}} \in L_{\infty}$ from (53). Based on (61), $\dot{\hat{\tau}} = -\dot{\hat{\tau}}$ is bounded because \hat{x} and f are bounded. Then, it can be concluded that $\dot{\chi}$ is bounded,

TABLE II SUMMARY OF OBSERVER DESIGN

System	Variables	Design Params.	Convergence Type
Surface			
Concentration	\check{c}_{ss}	L in (42)	Finite-Time
Observer			
Solid Phase	â	I in (52)	Agrimmtatia
Concentration	x	L_a in (53)	Asymptotic
Parameter -	$\hat{ au}$	a in (61)	Asymptotic
Diffusivity	7	γ in (61)	Asymptotic

which reveals that χ is uniformly continuous. Therefore, \dot{x} is uniformly continuous. Again, apply Barbalat's Lemma [47]

$$\lim_{t \to \infty} \dot{\tilde{x}} = 0. \tag{68}$$

Consider the first N state error dynamical equations in (56), and it implies that when $t \to \infty$

$$\tau \overline{\mathcal{A}} x - \hat{\tau} \overline{\mathcal{A}} \hat{x} + \tau \theta F(x) - \hat{\tau} \theta F(\hat{x}) \to 0.$$
 (69)

Theoretically, if the states converge asymptotically, i.e., $\hat{x} \to x$ as $t \to \infty$, then from (69), we have

$$[\overline{\mathcal{A}}x + \theta F(x)](\tau - \hat{\tau}) \to 0 \text{ as } t \to \infty.$$
 (70)

Therefore, $\hat{\tau}$ converges to τ asymptotically. The value which $\hat{\tau}$ converges to highly relies on whether \hat{x} provides an accurate estimation. In other words, the state estimation error determines how accurate the parameter estimation will be. The uncertainties in the adaptive observer may result from uncertainties in current and voltage measurements, and model mismatch. In addition, the performance of the adaptive observer is highly sensitive to the accuracy of the surface concentration observer since its output becomes the input of the adaptive observer. Any uncertainties in the surface concentration observer are passed into the adaptive observer stage.

C. Summary of Observer Design

The design of the complete observer is summarized in Table II. It lists equations for each subsystem, the corresponding design parameters, as well as the convergence type based on the analysis in Sections V-A and V-B.

VI. RESULTS AND DISCUSSION

In this section, we present results from simulation and experimental data to demonstrate the performance of the proposed nonlinear observers.

A. Simulation Study

The parameters used in the simulation are adopted from the DUALFOIL simulation package that is publicly available [48]. The model parameters for anode, including diffusion and mechanical properties, are enumerated in Table III. The mechanical parameters of anode material are obtained from [23]. We illustrate the observer performance by initializing the state and parameter estimates at incorrect values.

TABLE III
SPM-Stress Model Parameters

Symbols	Simulation	Experimental	Units
L^-	100×10^{-6}	123×10^{-6}	m
L^+	100×10^{-6}	119×10^{-6}	m
D_s^-	3.9×10^{-14}	7.98×10^{-16}	m ² /s
R_s^-	10×10^{-6}	8.21×10^{-6}	m
$egin{array}{c} arepsilon_s^- \ arepsilon_s^+ \ k^- \end{array}$	0.6	0.7215	N/A
$arepsilon_s^+$	0.5	0.6516	N/A
k^-	1×10^{-5}	2.19×10^{-6}	$A \cdot m^{2.5} / mol^{1.5}$
k^+	3×10^{-7}	2.68×10^{-7}	$A \cdot m^{2.5} / mol^{1.5}$
R_f	1.0×10^{-3}	1.0×10^{-3}	$\Omega \times m^2$
$n_{Li,s}$	2.5	0.14	mol
$c_{s,\mathrm{max}}^-$	24983	31168	mol/m ³
$c_{s,\max}^+$	46171	42649	mol/m ³
A	1	0.049	m^2
E_n	60	60	GPa
$ u_n$	0.25	0.25	N/A
Ω_n	4.926×10^{-6}	4.926×10^{-6}	m ³ /mol

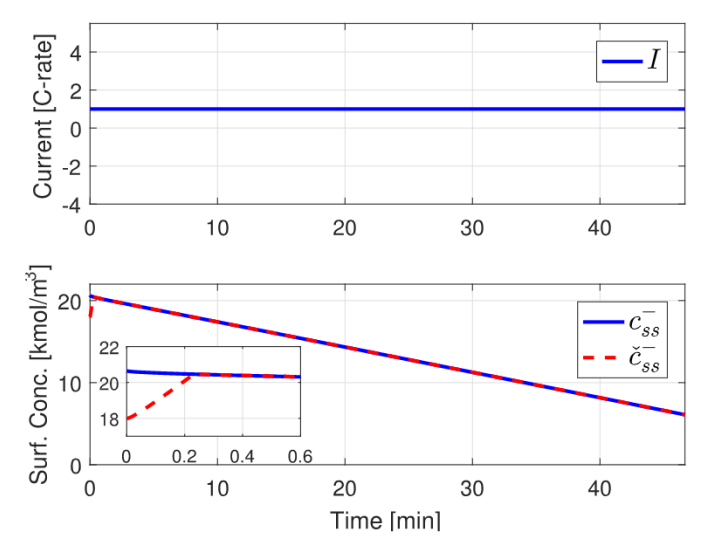


Fig. 4. Surface concentration observer results for a 1C constant current discharge. The estimate of surface concentration is initialized with incorrect value.

We apply a constant 1C discharge cycle for around 45 min. Fig. 4 portrays the evolution of input current and the surface concentration estimate from the surface concentration observer. The surface concentration estimation is initialized with a 12.8% error to validate the convergence property. Note that with a proper selection of the gain as presented in (48), the convergence time for \check{c}_{ss}^- is 15 s. Next, the surface concentration estimate is fed into the adaptive observer as a pseudomeasurement signal for combined state and parameter estimation. The estimation for surface concentration, terminal voltage, bulk SOC, and anode diffusivity is plotted against their simulated values from the plant model (23) in Fig. 5. Fig. 6 provides the plot of estimation for the maximum absolute radial and tangential stresses over time, which are located at the center and the surface of the anode electrode particle, respectively. With an appropriate choice of gain as presented in Sections V-A and V-B, the estimates effectively converge to their simulated values from the plant model. It is

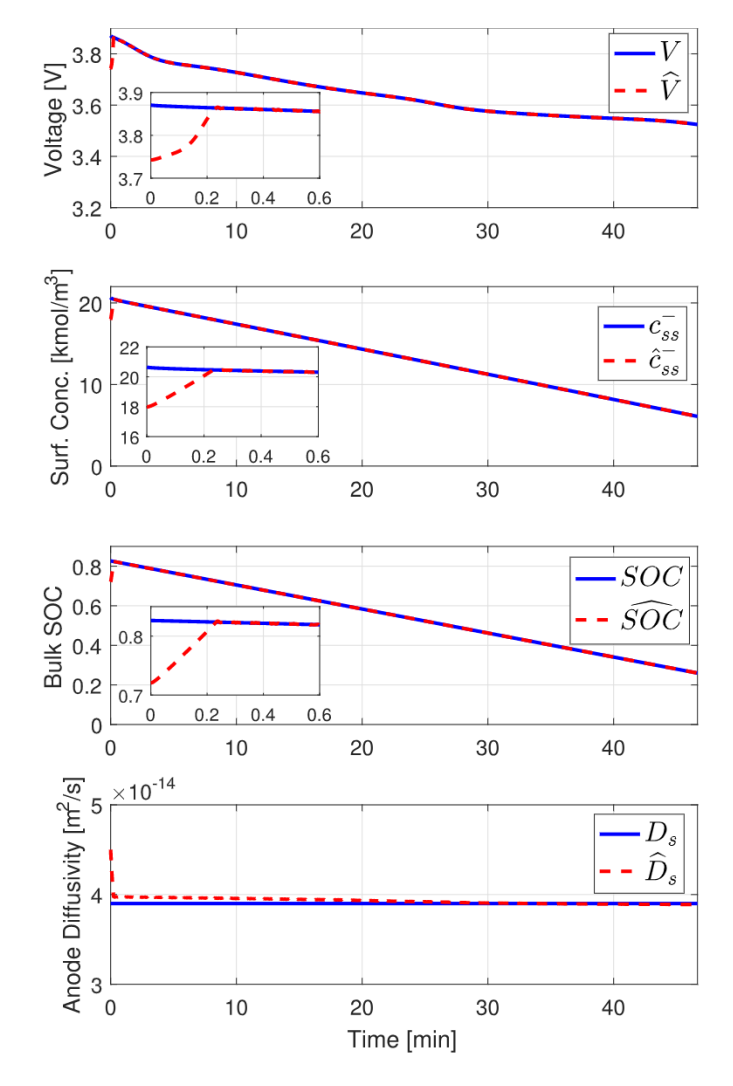


Fig. 5. Adaptive observer results for a 1C constant current discharge. The states and parameters converge to their true values asymptotically.

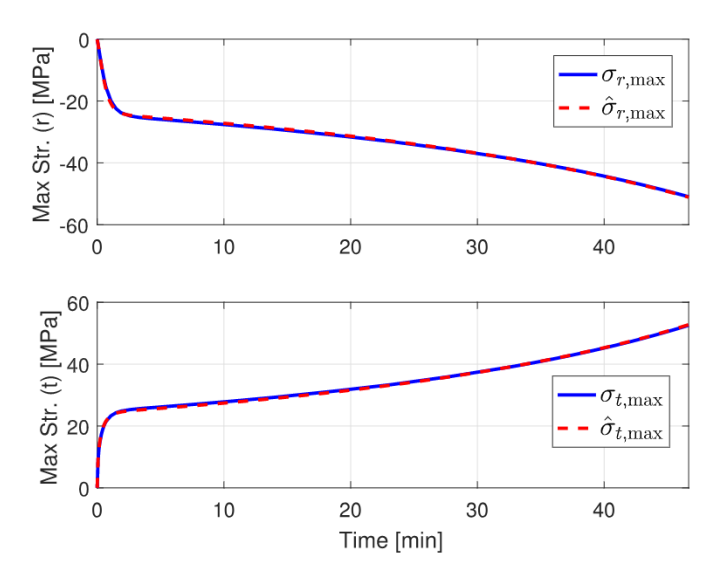


Fig. 6. Maximum radial and tangential stresses estimation under 1C discharge current.

worth mentioning that the internal stress estimates can be monitored in real time to prevent it from getting higher than the yielding stress of the electrode material, and utilized to analyze the stress-related physical degradation.

B. Experimental Studies

In this section, the performance of the designed adaptive observer is demonstrated via experimental data from a commercial LiNiMnCoO₂ (NMC)—LiC₆ cell. The ambient temperature of the battery cell under test is retained at 25.5 °C inside an ESPEC BTL-433 environmental chamber, and an Arbin high current cylindrical cell holder is used to hold the battery cell. A PEC SBT2050 cycler applies a vehicle chargedischarge cycle. The experimentally collected data, current, and voltage have been used for the identification of SPM-stress model parameters. For the model identification, we utilized particle swarm optimization (PSO) to minimize the root mean squared voltage error between experimental data and model output to get the best model fit [49]. Besides the parameters associated with battery geometry, mechanical properties, and equilibrium structure, the model parameters that are fitted by PSO are D_s^- , R_s^- , k^- , and k^+ . The mechanical parameters are adopted from [23] for graphite. A summary of the parameter values are listed in Table III. The state and parameter estimations are initialized with random (incorrect) guess to evaluate the convergence of the observers. Unlike the cases in the simulation study, we no longer know the true solid phase Li-ion concentration and SOC. Consequently, the criteria for assessing the observer performance is through the comparison of measured voltage and voltage estimates computed from Li-ion concentration estimation.

The "actual" quantities plotted in the figures are obtained through the following ways.

- 1) The "actual" diffusion coefficient is obtained by fitting the voltage output from the plant model in (23) to the experimental voltage measurement offline by PSO.
- 2) The "actual" surface concentration, maximum radial stress, and maximum tangential stress are simulated utilizing the plant model (23) with the identified parameters from the last step.
- The "actual" bulk SOC is computed by the coulomb counting technique, by integrating the applied current normalized with battery capacity.

During the experiment, the battery cell was first charged to 100% SOC using a standard constant—current—constant—voltage (CCCV) protocol, followed by a discharge period until the SOC drops down to 80% SOC. An electric vehicle like charge—discharge cycle is then applied to the battery cell, plotted in Fig. 7. The results for the surface concentration observer and adaptive observer are given in Figs. 7–9. The root mean squared percentage error (RMSPE) is selected to quantified the estimation accuracy

RMSPE
$$(z, \hat{z}) = \sqrt{\frac{1}{n} \sum_{i=1}^{n} \left(\frac{\hat{z}_i - z_i}{z_i} \times 100\%\right)^2}$$
 (71)

where z and \hat{z} denote the true and estimated quantities and n is the number of data points. After the initial transition period, the RMSPE between the voltage estimation and experimentally

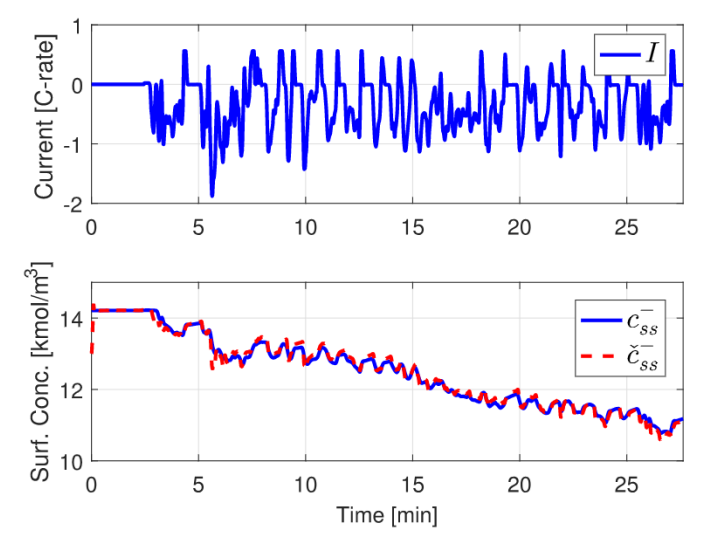


Fig. 7. Electric vehicle like charge–discharge cycle is applied to the battery cell. The surface concentration observer successfully tracks the surface concentration, compared against the simulated value from the model.

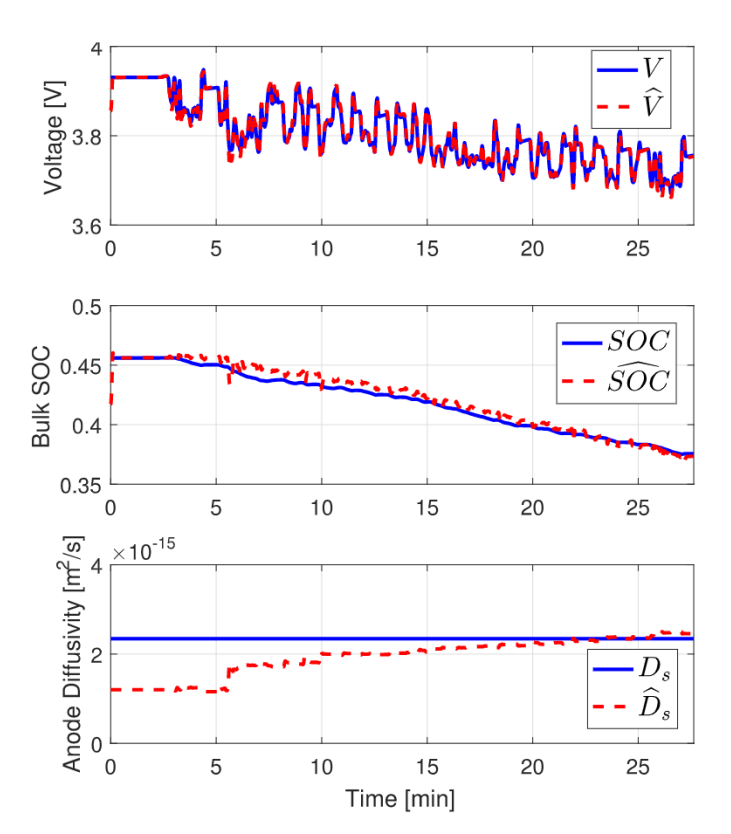


Fig. 8. Adaptive observer results for the charge–discharge cycle using experimental data. The "actual" SOC plotted in blue solid line is computed by coulomb counting method, and the "actual" diffusion coefficient in anode is obtained by fitting the voltage output from the plant model in (23) to the experimental voltage measurement offline using PSO.

measured voltage is 0.143%. Similarly, the RMSPE for SOC and anode diffusivity estimation against their true values is 1.24% and 5.53%, respectively. As expected, the estimated variables converge to their actual values starting with an incorrect initialization. Note that the estimated variables from the adaptive observer exhibit large uncertainties at the beginning,

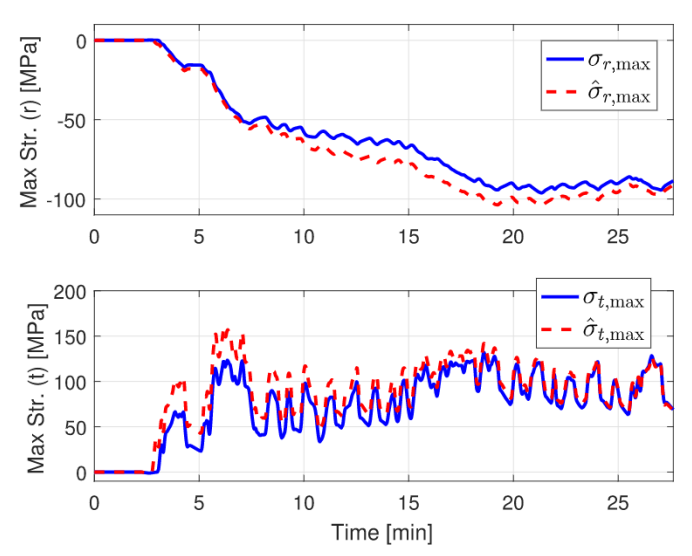


Fig. 9. Maximum radial and tangential stresses estimation in the using experimental data. The "actual" maximum radial stress, and maximum tangential stress are simulated utilizing the plant model (23) with the identified parameters.

mainly because the adaptive observer requires correct surface concentration estimation from the previous stage.

This paper presents and rigorously analyzes simultaneous state and parameter estimation utilizing the nonlinear coupled SPM and stress model. Similar to most other existing techniques [28], [42], the method proposed here is capable of estimating aging-related parameters in the battery model, e.g., diffusivity. Moreover, estimation of stresses generated inside the electrode particles provides another crucial measure for evaluating stress-related battery degradation phenomena.

Remark 6: This paper addresses observer design for nonlinear PDEs by projecting the PDEs onto a finite-dimension subspace, and applying nonlinear observer design for ODEs. For linear PDEs, one can avoid projection in the observer design by utilizing methods such as backstepping [50] or optimal estimation [51]. Unfortunately, a unified theory for nonlinear PDE observer design does not yet exist. Nevertheless, results can be obtained in special cases—a topic for future work.

VII. LIMITATION OF THE PROPOSED SCHEME

The adaptive estimation performance is reasonably well in the simulation study and using experimental data. Nonetheless, there are limitations in the proposed algorithm. In this section, we discuss and illustrate these limitations.

A. Flatness of Anode OCP

For the purpose of system observability, we reduce the coupled SPM and stress model by only considering the anode dynamics. A potential issue is that the OCP of the anode is generally flat, which means the sensitivity of output voltage with respect to the state is low. This may lead to large estimation error due to sensor and modeling uncertainties [52]. In order to compensate for the low sensitivity, observer with high gain is proposed. However, high gains amplify the output

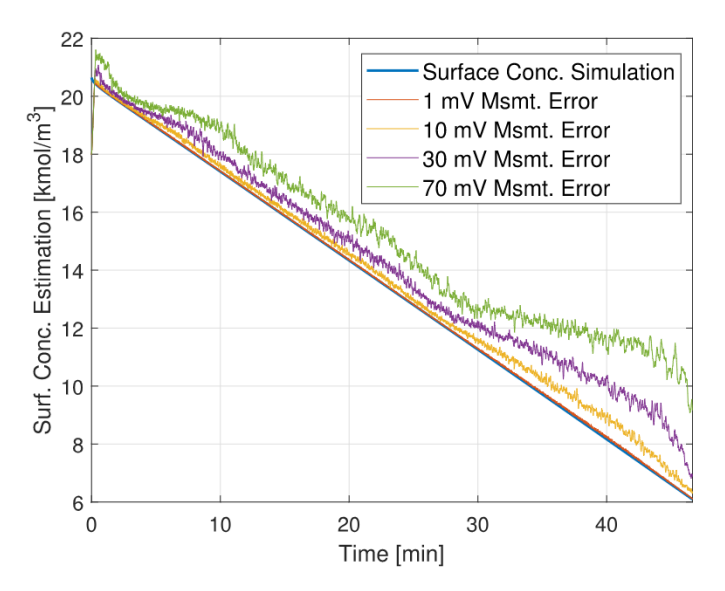


Fig. 10. Effect of measurement noise on the sliding mode observer in the surface concentration observer stage with constant input current (in simulation). Uniformly distributed noise with magnitudes of 1, 10, 30, and 70 mV is manually injected to the voltage signal.

measurement noise, but we expect the sliding mode observer to provide certain robustness. The effect of measurement noise on the sliding mode observer performance in the surface concentration observer stage is tested in the simulation with constant input current (see Fig. 10). Uniformly distributed noise with magnitudes of 1, 10, 30, and 70 mV is manually injected to the voltage signal. Due to the effect of high observer gain, the surface concentration estimation deviates from the actual (simulated) signal when uncertainties grow. This illustration reveals that the measurement uncertainty weakens the effectiveness of the estimation scheme owing to high observer gain.

B. Modeling Inadequacy

The coupled SPM and stress model adopted from [22] is derived from physical principles relying on an analogy to thermal stress and provides a quantitative aggregated stress prediction, which is useful to understand battery SOH associated with stress. This model has also desired computational simplicity for our application. However, the model is never validated against experimental data. It is derived based on the SPM, so: 1) it cannot capture the electrode localized stress as a function of position along the electrode and 2) its accuracy can be compromised for high input current, and electrolyte dynamics are expected to be incorporated as the electrode region in which fracture takes place depends on the electrolyte properties [53]. Moreover, reviewing the dynamical equation (6) and Remark 4, it is evident that the effects of temperature and concentration on θ^j and D_s^j were not taken into account. Finally, the model used here does not account for phase change and staging in the electrodes, which have a significant impact on the stress generation of some materials [27].

C. Unknown Actual Initial Condition

To compute the estimates $\hat{\sigma}_{r,\text{max}}$ and $\hat{\sigma}_{t,\text{max}}$ in real time, one needs to know the change of solid phase concentration estimation from the actual stress-free value, which is recognized as the concentration profile after relaxation. In the numerical studies in this paper, the "stress-free value of concentration" is simply the actual initial condition of the solid-phase concentration in the battery cell, and apparently, this information is unavailable. In the above-mentioned numerical studies (for instance see Fig. 7), zero current is injected at the beginning of an input profile, which allows: 1) the battery cell to relax and 2) the state observer to converge to the actual initial concentration instantly. The concentration estimation at the end of zero current can be used as the "actual" initial concentration. However, the convergence of observer within zero-current period is not guaranteed.

VIII. CONCLUSION

This paper presents a nonlinear observer for mechanical stress estimation in Li-ion batteries, along with solid-phase Li-ion concentration, i.e., SOC, and diffusion coefficient estimation. A key feature is utilizing an SPM coupled with an intercalation-induced stress model. Monitoring the mechanical response of electrode materials is crucial because particle fracture due to stress generation is a major source of battery capacity fade. The reduced PDE system for the SPM-stress model is approximated by nonlinear ODEs using the finite difference method. A nonlinear observer based on the sliding mode observer concept is proposed for estimating the surface concentration from current and voltage measurements only. The estimated surface concentration is then utilized as a pseudomeasurement signal for combined state and parameter estimation in the subsequent adaptive observer. The observers' convergence is mathematically proved using Lyapunov stability theory and Barbalat's Lemma. Real-time monitoring of aging-related parameters in battery model and internal mechanical stress enables: 1) a BMS to apply optimal control methods that protect against particle fracture, and consequently extend battery life and 2) further understanding of battery degradation behavior associated with diffusion-induced stress. Studies from simulation and experimental data are carried out to demonstrate observer performances. Future work seeks observer design on more advanced stress models.

REFERENCES

- N. A. Chaturvedi, R. Klein, J. Christensen, J. Ahmed, and A. Kojic, "Algorithms for advanced battery-management systems," *IEEE Control Syst. Mag.*, vol. 30, no. 3, pp. 49–68, Jun. 2010.
- [2] X. Hu, S. Li, and H. Peng, "A comparative study of equivalent circuit models for Li-ion batteries," *J. Power Sources*, vol. 198, pp. 359–367, Jan. 2012.
- [3] S. Santhanagopalan, Q. Guo, P. Ramadass, and R. E. White, "Review of models for predicting the cycling performance of lithium ion batteries," *J. Power Sources*, vol. 156, no. 2, pp. 620–628, 2006.
- [4] M. Doyle, T. F. Fuller, and J. Newman, "Modeling of galvanostatic charge and discharge of the lithium/polymer/insertion cell," *J. Electrochem. Soc.*, vol. 140, no. 6, pp. 1526–1533, 1993.
- [5] S. Santhanagopalan and R. E. White, "Online estimation of the state of charge of a lithium ion cell," *J. Power Sources*, vol. 161, no. 2, pp. 1346–1355, Oct. 2006.

- [6] D. Di Domenico, A. Stefanopoulou, and G. Fiengo, "Lithium-ion battery state of charge and critical surface charge estimation using an electrochemical model-based extended Kalman filter," J. Dyn. Syst., Meas., Control, vol. 132, no. 6, p. 061302, 2010.
- [7] N. Lotfi, R. Landers, J. Lie, and J. Park, "Electrochemical model-based adaptive estimation of Li-ion battery state of charge," in *Proc. ASME Dyn. Syst. Control Conf.*, 2015, p. V001T13A008.
- [8] S. K. Rahimian, S. Rayman, and R. E. White, "Extension of physics-based single particle model for higher charge-discharge rates," *J. Power Sources*, vol. 224, pp. 180–194, Feb. 2013.
- [9] S. J. Moura, F. B. Argomedo, R. Klein, A. Mirtabatabaei, and M. Krstic, "Battery state estimation for a single particle model with electrolyte dynamics," *IEEE Trans. Control Syst. Technol.*, vol. 25, no. 2, pp. 453–468, Mar. 2017.
- [10] T. R. Tanim, C. D. Rahn, and C.-Y. Wang, "State of charge estimation of a lithium ion cell based on a temperature dependent and electrolyte enhanced single particle model," *Energy*, vol. 80, pp. 731–739, Feb. 2015.
- [11] R. Klein, N. A. Chaturvedi, J. Christensen, J. Ahmed, R. Findeisen, and A. Kojic, "Electrochemical model based observer design for a lithium-ion battery," *IEEE Trans. Control Syst. Technol.*, vol. 21, no. 2, pp. 289–301, Mar. 2013.
- [12] A. Barré, B. Deguilhem, S. Grolleau, M. Gérard, F. Suard, and D. Riu, "A review on lithium-ion battery ageing mechanisms and estimations for automotive applications," *J. Power Sources*, vol. 241, pp. 680–689, Nov. 2013.
- [13] I.-S. Kim, "A technique for estimating the state of health of lithium batteries through a dual-sliding-mode observer," *IEEE Trans. Power Electron.*, vol. 25, no. 4, pp. 1013–1022, Apr. 2010.
- [14] D. Zhang, S. Dey, H. E. Perez, and S. J. Moura, "Remaining useful life estimation of lithium-ion batteries based on thermal dynamics," in *Proc. Amer. Control Conf. (ACC)*, 2017, pp. 4042–4047.
- [15] D. Zhang, S. Dey, H. E. Perez, and S. J. Moura, "Real-time capacity estimation of lithium-ion batteries utilizing thermal dynamics," *IEEE Trans. Control Syst. Technol.*, to be published.
- [16] S. J. Moura, N. Chaturvedi, and M. Krstic, "Adaptive PDE observer for battery SOC/SOH estimation," in *Proc. ASME Dyn. Syst. Control Conf.*, 2012, pp. 101–110.
- [17] S. Dey, B. Ayalew, and P. Pisu, "Adaptive observer design for a Li-ion cell based on coupled electrochemical-thermal model," in *Proc. ASME*, 2014, p. V002T23A001, Paper DSCC2014-5986.
- [18] S. Kalnaus, K. Rhodes, and C. Daniel, "A study of lithium ion intercalation induced fracture of silicon particles used as anode material in Li-ion battery," *J. Power Sources*, vol. 196, no. 19, pp. 8116–8124, 2011.
- [19] K. Aifantis and J. Dempsey, "Stable crack growth in nanostructured Li-batteries," J. Power Sources, vol. 143, no. 1, pp. 203–211, 2005.
- [20] R. Deshpande, Y. Qi, and Y.-T. Cheng, "Effects of concentration-dependent elastic modulus on diffusion-induced stresses for battery applications," J. Electrochem. Soc., vol. 157, no. 8, pp. A967–A971, 2010.
- [21] J. Christensen and J. Newman, "Stress generation and fracture in lithium insertion materials," J. Solid State Electrochem., vol. 10, no. 5, pp. 293–319, 2006.
- [22] X. Zhang, W. Shyy, and A. M. Sastry, "Numerical simulation of intercalation-induced stress in Li-ion battery electrode particles," *J. Elec*trochem. Soc., vol. 154, no. 10, pp. A910–A916, 2007.
- [23] J. Li, N. Lotfi, R. Landers, and J. Park, "A single particle model for lithium-ion batteries with electrolyte and stress-enhanced diffusion physics," J. Electrochem. Soc., vol. 164, no. 4, pp. A874–A883, 2017.
- [24] B. Suthar, V. Ramadesigan, S. De, R. D. Braatz, and V. R. Subramanian, "Optimal charging profiles for mechanically constrained lithium-ion batteries," *Phys. Chem. Chem. Phys.*, vol. 16, no. 1, pp. 277–287, 2013.
- [25] M. M. Forouzan, B. A. Mazzeo, and D. R. Wheeler, "Modeling the effects of electrode microstructural heterogeneities on Li-ion battery performance and lifetime," *J. Electrochem. Soc.*, vol. 165, no. 10, pp. A2127–A2144, 2018.
- [26] D. Zhang, S. Dey, and S. J. Moura, "Lithium-ion battery state estimation for a single particle model with intercalation-induced stress," in *Proc. Annu. Amer. Control Conf. (ACC)*, 2018, pp. 2294–2299.
- [27] J. Christensen and J. Newman, "A mathematical model of stress generation and fracture in lithium manganese oxide," *J. Electrochem. Soc.*, vol. 153, no. 6, pp. A1019–A1030, 2006.
- [28] J. Vetter et al., "Ageing mechanisms in lithium-ion batteries," J. Power Sources, vol. 147, no. 1, pp. 269–281, 2005.

- [29] M. Broussely et al., "Main aging mechanisms in Li ion batteries," J. Power Sources, vol. 146, nos. 1–2, pp. 90–96, 2005.
- [30] C. Lin, A. Tang, N. Wu, and J. Xing, "Analysis for mechanical failure of diss with graphite anode in lithium ion batteries for electric vehicles," *Nanomater. Nanotechnol.*, vol. 6, pp. 1–7, Jul. 2016.
- [31] P. Barai, K. Smith, C.-F. Chen, G.-H. Kim, and P. P. Mukherjee, "Reduced order modeling of mechanical degradation induced performance decay in lithium-ion battery porous electrodes," *J. Electrochem. Soc.*, vol. 162, no. 9, pp. A1751–A1771, 2015.
- [32] T. Meurer, "On the extended luenberger-type observer for semilinear distributed-parameter systems," *IEEE Trans. Autom. Control*, vol. 58, no. 7, pp. 1732–1743, Jul. 2013.
- [33] A. Smyshlyaev and M. Krstic, Adaptive Control Parabolic of PDEs. Princeton, NJ, USA: Princeton Univ. Press, 2010.
- [34] T. Ahmed-Ali, F. Giri, M. Krstic, L. Burlion, and F. Lamnabhi-Lagarrigue, "Adaptive boundary observer for parabolic PDEs subject to domain and boundary parameter uncertainties," *Automatica*, vol. 72, pp. 115–122, Oct. 2016.
- [35] P. Ascencio, "Adaptive observer design for parabolic partial differential equations," Ph.D. dissertation, Dept. Elect. Electron. Eng., Imperial College London, London, U.K., 2017.
- [36] S. Dey, B. Ayalew, and P. Pisu, "Nonlinear adaptive observer for a lithium-ion battery cell based on coupled electrochemical-thermal model," ASME J. Dyn. Syst., Meas. Control, vol. 137, no. 11, p. 111005, Aug. 2015.
- [37] X. Lin, A. G. Stefanopoulou, Y. Li, and R. D. Anderson, "State of charge imbalance estimation for battery strings under reduced voltage sensing," *IEEE Trans. Control Syst. Technol.*, vol. 23, no. 3, pp. 1052–1062, May 2015.
- [38] S. Zhao, S. R. Duncan, and D. A. Howey, "Observability analysis and state estimation of lithium-ion batteries in the presence of sensor biases," *IEEE Trans. Control Syst. Technol.*, vol. 25, no. 1, pp. 326–333, Jan. 2017.
- [39] M. Vidyasagar, Nonlinear Systems Analysis, vol. 42. Philadelphia, PA, USA: SIAM, 2002.
- [40] R. Deshpande, M. Verbrugge, Y.-T. Cheng, J. Wang, and P. Liu, "Battery cycle life prediction with coupled chemical degradation and fatigue mechanics," *J. Electrochem. Soc.*, vol. 159, no. 10, pp. A1730–A1738, 2012.
- [41] M. Safari, M. Morcrette, A. Teyssot, and C. Delacourt, "Life-prediction methods for lithium-ion batteries derived from a fatigue approach i. introduction: capacity-loss prediction based on damage accumulation," *J. Electrochem. Soc.*, vol. 157, no. 6, pp. A713–A720, 2010.
- [42] L. Zhang, L. Wang, C. Lyu, J. Li, and J. Zheng, "Non-destructive analysis of degradation mechanisms in cycle-aged graphite/LiCoO2 batteries," *Energies*, vol. 7, no. 10, pp. 6282–6305, 2014.
- [43] Y. M. Cho and R. Rajamani, "A systematic approach to adaptive observer synthesis for nonlinear systems," *IEEE Trans. Autom. Control*, vol. 42, no. 4, pp. 534–537, Apr. 1997.
- [44] R. Marino, "Adaptive observers for single output nonlinear systems," IEEE Trans. Autom. Control, vol. 35, no. 9, pp. 1054–1058, Sep. 1990.
- [45] Y. Shtessel, C. Edwards, L. Fridman, and A. Levant, "Introduction: Intuitive theory of sliding mode control," in *Sliding Mode Control Observation*. New York, NY, USA: Springer, 2014, pp. 1–42.
- [46] H. K. Khalil, Noninear Systems, vol. 2. Upper Saddle River, NJ, USA: Prentice-Hall, 1996, no. 5, pp. 1–5.
- [47] K. S. Narendra and A. M. Annaswamy, Stable Adaptive Systems. Chelmsford, MA, USA: Courier Corporation, 2012.
- [48] J. Newman. (2004). Fortran Programs for Simulation of Electrochemical Systems, Dualfoil. F Program for Lithium Battery Simulation. [Online]. Available: www.cchem.berkeley.edu/jsngrp/fortran.html
- [49] S. Ebbesen, P. Kiwitz, and L. Guzzella, "A generic particle swarm optimization MATLAB function," in *Proc. Amer. Control Conf. (ACC)*, 2012, pp. 1519–1524.
- [50] M. Krstic and A. Smyshlyaev, Boundary Control of PDEs: A Course on Backstepping Designs, vol. 16. Philadelphia, PA, USA: SIAM, 2008.
- [51] S. J. Moura and H. K. Fathy, "Optimal boundary control & Estimation of diffusion-reaction PDEs," in *Proc. Amer. Control Conf. (ACC)*, 2011, pp. 921–928.
- [52] X. Lin and A. G. Stefanopoulou, "Analytic bound on accuracy of battery state and parameter estimation," *J. Electrochem. Soc.*, vol. 162, no. 9, pp. A1879–A1891, 2015.
- [53] J. Christensen, "Modeling diffusion-induced stress in Li-ion cells with porous electrodes," J. Electrochem. Soc., vol. 157, no. 3, pp. A366–A380, 2010.

Dong Zhang received the B.S. degree in civil and environmental engineering from the University of Michigan, Ann Arbor, MI, USA, in 2015, the B.S. degree in electrical and computer engineering from Shanghai Jiao Tong University, Shanghai, China, in 2015, and the M.S. degree from the University of California at Berkeley, CA, USA, in 2016, where he is currently pursuing the Ph.D. degree.

His current research interests include energy systems, battery management system designs, and estimation and control for nonlinear and infinite-dimensional dynamical systems. He has been nominated for the Energy Systems Best Student Paper Award at the 2018 IEEE American Control Conference. He is also a recipient of the UC Berkeley College of Engineering Block Grant Award.

Satadru Dey (S'13–M'15) received the master's degree in control systems from IIT Kharagpur, Kharagpur, India, in 2010, and the Ph.D. degree in automotive engineering from Clemson University, Clemson, SC, USA, in 2015. From 2010 to 2012, he was a Control Engineer at General Electric Company, Hyderabad, India. He was a Post-Doctoral Researcher at the University of California, Berkeley, CA, USA, from 2015 to 2017. He is currently an Assistant Professor of electrical engineering with the University of Colorado, Denver, CO, USA. His technical background is in the area of controls. His current research interests include energy and transportation systems, developing control, estimation and diagnostics algorithms for batteries, ultracapacitors, fuel cells, electric vehicles, and connected and autonomous vehicles.

Luis D. Couto received the bachelor's degree in chemical engineering from Simón Bolívar University, Caracas, Venezuela, in 2013, the master's degree in renewable energies from the Autonomous University of Madrid, Spain, in 2014, and the Ph.D. degree from the Université Libre de Bruxelles, Belgium, in 2018. He is currently a Post-Doctoral Researcher with the Department of Control Engineering and System Analysis, Université Libre de Bruxelles, Belgium. His current research interests include state/parameter estimation, fault diagnosis and optimal control in the context of battery-management systems.

Scott J. Moura (S'09–M'13) received the B.S. degree from the University of California, Berkeley, CA, USA, and the M.S. and Ph.D. degrees from the University of Michigan, Ann Arbor, MI, USA, in 2006, 2008, and 2011, respectively, all in mechanical engineering.

He is currently an Assistant Professor and the Director of the Energy, Controls, & Applications Lab (eCAL) in Civil & Environmental Engineering with the University of California, Berkeley, CA, USA. He is also an Assistant Professor with the Smart Grid and Renewable Energy Laboratory, Tsinghua-Berkeley Shenzhen Institute. From 2011 to 2013, he was a Post-Doctoral Fellow at the Cymer Center for Control Systems and Dynamics, University of California, San Diego, CA, USA. In 2013, he was a Visiting Researcher at the Centre Automatique et Systems, MINES ParisTech, Paris, France. His current research interests include control, optimization, and machine learning for batteries, electrified vehicles, and distributed energy resources.

Dr. Moura was a recipient of the National Science Foundation Graduate Research Fellowship, the UC Presidential Postdoctoral Fellowship, the O. Hugo Shuck Best Paper Award, the ACC Best Student Paper Award (as advisor), the ACC and ASME Dynamic Systems and Control Conference Best Student Paper Finalist (as student), the Hellman Fellows Fund, the University of Michigan Distinguished ProQuest Dissertation Honorable Mention, the University of Michigan Rackham Merit Fellowship, and the College of Engineering Distinguished Leadership Award.